International Journal of Heat and Mass Transfer 261 (2026) 128580

Contents lists available at ScienceDirect

International Journal of Heat and Mass Transfer

journal homepage: www.elsevier.com/locate/hmt

Multidimensional modeling of reference PEM fuel cells from the European Joint Research Centre

Carmine Marra [a,*], Marcos López Juárez [b], Giacomo Filippini [a], Ricardo Novella [b], Stefano Fontanesi [a], Alessandro d'Adamo [a]

[a] University of Modena and Reggio Emilia, Engineering Department "Enzo Ferrari", Via Università 4, Modena, 41121, MO, Italy
[b] CMT-Clean Mobility & Thermofluids, Universitat Politècnica de València, Cami de Vera s/n, 46022, Valencia, Spain

ARTICLE INFO

Keywords:
3D-CFD simulation of polymeric exchange membrane fuel cells
Effects of hardware design in MEA testing
Membrane water management

ABSTRACT

The absence of standardized hardware hinders consistent membrane electrode assembly characterization in proton exchange membrane fuel cells. To address this, the European Joint Research Centre established two reference configurations: the Single-Serpentine Testing Hardware (SSHW) and the ZeroVCell (ZGC).

While experimental studies demonstrated the superior performance of the ZGC, the underlying physical mechanisms have not yet been fully clarified. In this work, three-dimensional computational fluid dynamics simulations were performed to reproduce and interpret the operation of both cells, elucidating operational aspects inaccessible for direct measurements. The models were initially validated against the available experimental data, and then used to provide spatially resolved insights into the interplay between electrochemical kinetics, mass transport, and water management.

A novel flux-decomposition sub-model is implemented to decouple electro-osmotic drag from back-diffusion, enabling spatially resolved quantification of hydration dynamics inaccessible to direct measurement. Overpotentials are dissected to indicate the dominant loss type, with simulation results confirming that the ZGC configuration exhibits lower ohmic and mass transport losses than the SSHW, thanks to its more uniform hydration and reactant distribution combined with a larger area for current conduction, whereas the SSHW is subject to a relevant oxygen depletion and to intense anode dehydration, leading to increased ohmic and mass transport overpotentials.

Beyond the comparison of the two hardware designs, this study focuses on the capability of the developed modeling framework to extend the understanding of cell's hard-to-quantify quantities (e.g., spatial distributions, membrane water flux decomposition, overpotentials breakdown), offering a robust complementary methodology for the design, optimization, and standardization of testing protocols.

1. Introduction

Significant progress has been made in proton exchange membrane fuel cells (PEMFCs) over the past decade, making them promising candidates for both transportation and small stationary applications because of their high electrical efficiency, power density, and durability. However, their large-scale commercialization remains restricted by the high system costs and the slow pace of component and infrastructure development [1].

PEMFCs are complex electrochemical reactors that convert the chemical energy of hydrogen into electrical power, with low-temperature heat and water as the only by-products. Their operation is based on the coupled interaction of electrochemical reactions, heat and mass transfer, with multiphase flows within porous electrodes and channels. This generates a set of concurrent transport processes for fluids, energy, and charges (i.e., currents). Understanding and quantifying these interactions is essential to improve the cell design, the durability, and the overall efficiency, although their local measurement is often experimentally not possible.

A key aspect for PEMFC optimal operation is to maintain an adequate and uniform membrane hydration level, to ensure proton conductivity and prevent degradation. Conventional fuel cell systems use external humidifiers to precondition the inlet gases, adding cost and complexity. A more convenient solution would be the self-humidification of the cell where water produced in the cathode is recirculated through the membrane by electro-osmotic drag and diffusive back-transport offering a more compact solution. However, this scenario would require

* Corresponding author.
E-mail address: carmine.marra@unimore.it (C. Marra).

https://doi.org/10.1016/j.ijheatmasstransfer.2026.128580
Received 31 October 2025; Received in revised form 4 February 2026; Accepted 19 February 2026

an accurate analysis of the individual processes at the origin of the net water transport across the polymeric membrane, which are often not accessible for direct measurement. Therefore, modeling these interfacial fluxes becomes essential for predicting the membrane water management and the resulting cell's performance.

In [2,3], an extensive experimental campaign was conducted at the European Union Joint Research Centre (JRC). Two cell architectures were compared: a serpentine single-channel flow field (Single-Serpentine Hardware, SSHW) operated at low stoichiometry (SR_a = 1.3, SR_c = 1.5), aiming at representing a common laboratory-scale test cell, and a parallel-channel configuration (Zero-Gradient Cell, ZGC) operated at high stoichiometry (SR_a = 8.0, SR_c = 10.0), designed to ensure uniform operating conditions across the membrane electrode assembly (MEA). The authors in [2,3] experimentally characterized both cells using polarization curves and in-situ diagnostics, particularly electrochemical impedance spectroscopy (EIS), which enables the decomposition of total overpotentials into their kinetic, ohmic, and mass transport contributions based on the different frequency response. Although EIS provides valuable macroscopic insights into the cell' loss types [4,5], it cannot resolve the spatial distribution of physical quantities and is subject to possible anode–cathode disturbance for specific losses. Consequently, it might be not suitable to indicate the underlying causes of processes such as localized flooding, membrane dehydration, or non-uniform current density.

To complement the experimental analyses, numerical modeling, particularly three-dimensional computational fluid dynamics (3D-CFD), has emerged as a powerful approach to investigate PEMFCs's behavior. This class of models is based on differential equations to represent the coupled transport of mass, energy, charge, and species, providing detailed information on electrochemical reaction rates, liquid water accumulation, and membrane hydration levels. In particular, the accurate prediction of liquid water distribution is critical for identifying areas of sub-optimal operation and for designing improved flow-field and operating strategies [6,7].

While PEMFC CFD modeling is a well-established field, the novelty of this study lies in two distinct areas: (i) the methodological implementation of water transport analysis through the polymeric membrane, and (ii) the application to reference standardization hardware to integrate and extend the benchmark cases proposed by the JRC.

First, regarding the flux-decomposition methodology, a custom sub-model was implemented to decouple the global net water transport into its two competing components: EOD and BD. Unlike standard commercial CFD codes that typically resolve only the net flux, the proposed approach allows for the spatially resolved quantification of these opposing fluxes, providing deeper insights into hydration dynamics.

Second, this study provides a comprehensive 3D-CFD multidimensional analysis of the SSHW and ZGC developed by the European Joint Research Centre. The numerical interpretation of why the ZGC outperforms the SSHW, specifically regarding the spatial distribution of membrane water content and local overpotential breakdown, constitutes a novel contribution that complements experimental testing results with non-measurable insights and supports the international effort toward testing standardization.

The objectives of this study are (i) to simulate the operation of the two hardware configurations developed by the JRC to validate the numerical predictions against the measured experimental data from [2,3], and (ii) to apply the implemented flux-decomposition sub-model to identify and quantify the dominant water transport mechanisms across the membrane under different operating regimes. The present work aims at deepening the understanding of the physical mechanisms that distinguish the operation of the SSHW and ZGC, assessing how hardware design and stoichiometric choices affect local hydration and mass transport levels, and demonstrating the potential of detailed multiphysics modeling to complement experimental campaigns for quantities inaccessible to measurements.

The proposed modeling framework bridges the knowledge gap between testing best-practices and a complete understanding of PEMFC operation, promoting a unified experimental–numerical methodology capable of providing both global and spatially-resolved insights into PEMFC processes, thereby supporting the development of more efficient and reproducible testing strategies across research institutions.

2. Mathematical model

In this study, the commercial CFD software Simcenter STAR-CCM+ (Siemens Digital Industries Software) has been used to develop a multiphysics, non-isothermal and multi-phase modeling of the SSHW and ZGC. The low-temperature regime of PEMFC implies the introduction of a multiphase fluid model. In this study, the Mixture Multiphase model (MMP) has been adopted to this aim, with the hypothesis that the gas and liquid phases are fully miscible and in local thermodynamic equilibrium, allowing their motion to be representable as that of an equivalent single-phase fluid. Within this framework, a single set of transport equations is solved for the conservation of mass, momentum, energy, and charges (electrons and ions), while additional equations are used to compute the phase volume fraction and the relative velocity between phases. This method provides the simplest yet comprehensive formulation for capturing the fundamental conservation and transport phenomena occurring in PEMFCs. Due to its balance between physical realism and computational efficiency, the MMP model has been widely adopted in the literature and has significantly contributed to the advancement of CFD-based PEMFC modeling [8]. For the sake of conciseness, only a brief description of the adopted model is provided here, while a detailed explanation can be found in [9].

The governing equations for the MMP model are reported in Table 1, and the following assumptions are used in their derivation [10]:

1. Laminar flows.
2. Ideal gases.
3. Neglected gravity field.
4. Porous parts (Gas Diffusion Layers, GDLs, and Catalyst Layers, CLs) modeled with a macro-homogeneous approach, characterized by effective integral properties, function of the local porosity (ε).
5. Steady-state processes.

The modeling of the diffusion media (GDLs and CLs) adopts the macro-homogeneous approach, assuming a uniform microstructure of equally sized and spaced carbon fibers. This method is the dominant choice in the specific literature, as (i) it overcomes the modeling of the complex fibrous structure of the material, whose details are often unknown, and (ii) it incorporates integral terms to approximate the large-scale effects of the presence of the solid phase. The key parameters in this approach include porosity, i.e. the ratio of pores to total volume, and tortuosity, defined as the ratio of the convoluted path to the theoretical straight-line distance, as given by Eq. (6) [11]. Other large-scale integral properties include the absolute permeability (i.e. momentum conductance) and the effective thermal/electrical conductivity, leveraging component-oriented empirical data without the need to directly represent their complex three-dimensional solid/void morphology.

$$\tau = \left(\frac{1}{\varepsilon}\right)^{0.5} \tag{6}$$

Eqs. (1) and (2) represent the conservation of mass and momentum for the equivalent fluid, with ε being the porosity of the porous medium, and ρ_{mix} and V_{mix} the density and velocity of the fluid mixture, respectively. The term S_m in Eq. (7) considers for the species conversion to/from charges (i.e., electrons and ions) due to the electrochemical reactions.

In Eq. (2), in addition to the pressure gradient (∇p) and the viscous resistance expressed by the molecular viscosity (μ), the effect of the

Table 1
Steady-state governing equations used in the MMP model.

Performance measure	Definition	Eq.
Continuity Equation	$\nabla \cdot (\varepsilon \rho_{mix} \vec{V}_{mix}) = S_m$	(1)
Momentum Equation	$\nabla \cdot (\rho_{mix} \varepsilon^2 \vec{V}_{mix} \vec{V}_{mix}) = -\nabla p + \nabla(\mu \varepsilon \nabla \cdot \vec{V}_{mix}) + \vec{S}_V + \vec{S}_{cap}$	(2)
Species Equation	$\nabla \cdot (\rho_{mix} Y_k \varepsilon \vec{V}_{mix}) = \nabla \cdot (\rho D_k^{eff} \nabla Y_k) + \vec{S}_k$	(3)
Internal Energy Equation	$\nabla \cdot [(\rho_{mix} c_p)^{eff} T \varepsilon \vec{V}_{mix}] = \nabla \cdot (k^{eff} \nabla T) + S_T$	(4)
Charge Equations	$0 = \nabla \cdot (\sigma_s^{eff} \nabla \Phi_s) + S_{\Phi_s}$; $0 = \nabla \cdot (\sigma_e^{eff} \nabla \Phi_e) + S_{\Phi_e}$	(5)

flow resistance of the porous material is considered with the term S_V (Eq. (8)), where, κ is the effective permeability and is calculated as the product of the absolute permeability (K) of the porous medium and the relative phase permeability of the porous matrix (K_{rl}) [12]. In addition, the capillary pressure of the porous regions is modeled using an empirical Leverett [12] function based on the local liquid volume fraction (χ_l) gradient, as in Eq. (9). This function is applied both to the GDLs and to the CLs, with specific properties in each part.

$$S_m = \sum_k S_k \tag{7}$$

$$\vec{S}_V = -\frac{\mu}{\kappa} \vec{V}_{mix} \tag{8}$$

$$\vec{S}_{cap} = \gamma cos(\theta) \sqrt{\frac{\varepsilon}{K}} \nabla \cdot \left(1.417 \chi_l - 2.120 \chi_l^2 + 1.263 \chi_l^3\right) \tag{9}$$

The steady-state conservation equation for the mass fraction Y_k of the k-th species is expressed by Eq. (3), where the source term at CLs (S_k) is calculated from the Faraday's law as in Eq. (10), with z_k being the number of transferred charges per molecule of reactant/product, F the Faraday's constant, and M_k the species molecular weight. Moreover in Eq. (3) the diffusion term utilizes an effective diffusivity coefficient (D_i^{eff}), calculated from the value at standard conditions and then modified based on the local pressure and temperature. This is multiplied by $\varepsilon^{1.5}$ (Bruggemann's correction), reproducing the slower diffusion process observed in porous media. In Eq. (10), j represents the volumetric current density described by the Butler–Volmer equation which is applied both at the cathode (Eq. (12)) and the anode (Eq. (11)).

$$S_k = \pm \frac{j}{z_k F} M_k \tag{10}$$

$$j_a = \zeta_a \cdot j_{0,a}^{ref} \cdot \left(\frac{c_{H_2}}{c_{H_2}^{ref}}\right) \cdot \left[\exp\left(\frac{\alpha_a F \eta_a}{RT}\right) - \exp\left(\frac{-\alpha_c F \eta_a}{RT}\right)\right] \tag{11}$$

$$j_c = \zeta_c \cdot j_{0,c}^{ref} \cdot \left(\frac{c_{O_2}}{c_{O_2}^{ref}}\right) \cdot \left[-\exp\left(\frac{\alpha_a F \eta_c}{RT}\right) + \exp\left(\frac{-\alpha_c F \eta_c}{RT}\right)\right] \tag{12}$$

Unlike GDLs, CLs host the electrochemical reactions, hence their modeling requires the inclusion of the electrochemical activity of the supported Pt/C agglomerates. The macro-homogeneous model allows the simulation of electrochemical reactions on a statistically convoluted solid–fluid interface, which is larger than the corresponding planar area, thus introducing the Electrochemical Active Specific Area (ECSA) and the concept of a volumetric reaction rate [13]. The terms ζ_a and ζ_a represent the catalyst ECSA, modeled as in Eqs. (13) and (14) for the anodic and cathodic catalyst layers (ACL and CCL, respectively):

$$\zeta_a = \frac{A_s^a m_{Pt}^a}{\delta_{CL}^a} \qquad \text{in the ACL} \tag{13}$$

$$\zeta_c = \frac{A_s^c m_{Pt}^c}{\delta_{CL}^c} \qquad \text{in the CCL} \tag{14}$$

The term A_s (Eq. (15)) depends on the catalyst deposition on the graphite support and it can be related to the mass fraction of platinum (f) [14]:

$$A_s = (227.79 f^3 - 158.57 f^2 - 201.53 f + 159.5) \cdot 10^{-3} \tag{15}$$

Moreover, the volume fractions of the three phases in CL are obtained via Eqs. (16), (17), and (18) [15], where m_{Pt} denotes the loading of platinum, δ_{CL} the thickness of CL, and ρ_{Pt}, ρ_C, ρ_{im} and ρ_w denote the densities of platinum, carbon, ionomer phase and liquid water, respectively. In addition, the mass fraction of ionomer and platinum are represented by $\zeta_{im/C}$ and $\zeta_{Pt/C}$, and EW, λ_{mem} and M_w represent the equivalent molecular weight of the ionomer phase, the amount of water present in the membrane and the molecular mass of the water.

$$\chi_{Pt/C} = \frac{m_{Pt}}{\delta_{CL}} \left[\frac{1}{\rho_{Pt}} + \left(\frac{1}{\zeta_{Pt/C}} - 1\right) \frac{1}{\rho_C}\right] \tag{16}$$

$$\chi_{im} = \frac{\zeta_{im/C} m_{Pt}}{\delta_{CL} \rho_{im}} \left(\frac{1}{\zeta_{Pt/C}} - 1\right) \left(1 + \frac{M_w \rho_{im}}{\rho_w EW} \lambda_{mem}\right) \tag{17}$$

$$\chi_{CL} = 1 - \chi_{Pt/C} - \chi_{im} \tag{18}$$

In Eqs. (11) and (12), $j_{0,a}^{ref}$ and $j_{0,c}^{ref}$ represent the reference exchange current densities at anode and cathode, while α_a and α_c are the anodic and cathodic charge transfer coefficients and η_a and η_c are the activation overpotentials of the reactions.

Another physical process to consider is the liquid–vapor phase transition. This can be computed assuming local thermodynamic equilibrium, with various formulations available in the literature [16,17]. In this work, the model described in [18] has been applied for this purpose, and it considers the mass transfer rate during condensation and evaporation as in Eq. (19), where k_C $[1/s]$ and k_E $[1/Pa \cdot s]$ are condensation and evaporation rate constants, x is the water mole fraction, ρ_l is the density of the liquid phase and M_w is the water molar weight. The phase transition involves the release or absorption of heat, and the corresponding heat source term that is expressed by Eq. (20), with the latent heat of evaporation of water (H_{lat}) calculated as in Eq. (21).

$$\dot{m} = \begin{cases} k_C \cdot (1 - \chi_l) \cdot \frac{M_w}{RT} \cdot p \cdot (x_w^g - x_{w,sat}) & \text{if } x_{w,sat} \le x_w^g \\ k_E \cdot \chi_l \cdot \rho_l \cdot p \cdot (x_w^g - x_{w,sat}) & \text{if } x_{w,sat} > x_w^g \end{cases} \tag{19}$$

$$Q = \dot{m} H_{lat} \tag{20}$$

$$H_{lat} = 307090 \cdot (647.15 - T)^{0.35549} \tag{21}$$

The steady-state form of the internal energy conservation equation (Eq. (4)) consists of an thermal energy advective capacity and thermal conductivity, which are the volume-weighted averages of the fluid- and solid-phase specific heat and thermal conductivity, respectively. Furthermore, the term S_T (Eq. (22)) accounts for the heat generation due to the concurrent Joule effect of both the ionic (i_e) and the electronic current (i_s), the exothermal chemical reactions, and to the electrochemical activation losses at electrodes.

$$S_T = \frac{i_s^2}{k^{eff}} + \frac{i_e^2}{\sigma^{eff}} + j_a \eta_{act} + j_a \frac{T \Delta S}{2F} \tag{22}$$

The ions and electrons generated during the electrochemical reactions lead to the formation of an ionic (Φ_e) and electronic (Φ_s) potential field. The transport of electrons and ions (s and e subscript, respectively) is governed by Eq. (5), where σ_s^{eff} and σ_e^{eff} represent their respective charge conductivity coefficients and S_{Φ_s} and S_{Φ_e} the corresponding sources of electronic and ionic potential, related to the volumetric current density.

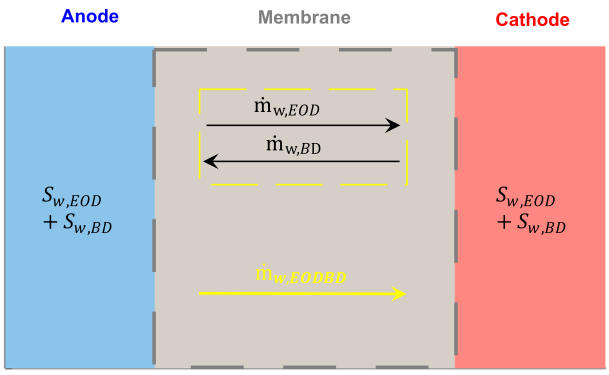

Fig. 1. Schematic of the water transport mechanisms across the membrane and their numerical coupling via source terms.

2.1. Membrane modeling

The polymeric electrolyte membrane is modeled as an impermeable solid that allows the transport of ionic charges (migration), with all its properties reflecting those of the Nafion polymer (DuPont® Nafion, New Castle, DE, USA), as reported by Springer et al. [19]. In this study, the diffusive model widely employed in PEMFC CFD simulations [12] is adopted to describe species transport within the solid medium. Specifically, two species are considered: protons (i.e., positive ions) and dissolved water. The proton flux is driven by the ionic potential gradient and it is directly proportional to the proton diffusivity, whereas the dissolved water transport is driven by the water concentration gradient and the diffusion coefficient in the dissolved phase. More details on the implementation of this model can be found in the authors' previous work [6].

To accurately predict the ionic conductivity of the membrane, it is essential to correctly determine both the local membrane water content and temperature. The ionic conductivity is derived from a semi-empirical correlation for a perfluorosulfonic polymer expressed as Eq. (23) from Springer et al. [19], where the membrane water content (λ_{mem}) is calculated based on Eq. (24), with the water activity expressed as in Eq. (25):

$$\sigma^{eff} = (0.5139\lambda_{mem} - 0.326) \cdot e^{[1268(\frac{1}{303} - \frac{1}{T})]} \tag{23}$$

$$\lambda_{mem} = \begin{cases} 0.043 + 17.81a - 39.85a^2 + 36a^3 & 0 < a_m \leq 1 \\ 14 + 1.4(a-1) & 1 \leq a_m \leq 3 \end{cases} \tag{24}$$

$$a = \frac{c_w RT}{p^{sat}} \tag{25}$$

As reported in the introduction section, an effective water management strategy must prevent both flooding and dehydration across the active area. Given the significance of this phenomenon, an in-house model for membrane water transport has been developed to separate the electro-osmotic drag and back diffusion fluxes, as it will be described in the following sections.

2.1.1. Water transport across the membrane

Effective water management is governed by the net transport across the membrane, resulting from the interplay between Electro-osmotic Drag (EOD) and Back-Diffusion (BD). In this numerical framework, these physical transport mechanisms are mathematically coupled to the porous electrode domains via volumetric source and sink terms applied to the CLs, as schematically illustrated in Fig. 1.

Membrane hydration is primarily promoted by the cathode-oriented migration of protons through the Nafion polymer pores. This phenomenon, known as EOD, drives a water mass flux directed from the anode to the cathode. The magnitude of this flux depends on the EOD coefficient (n_d), defined as the statistical number of water molecules dragged per proton transported. The coefficient is calculated using the correlation reported by Carcadea et al. [20] and shown in Eq. (26).

$$n_d = 0.0528\lambda_{mem} - 3.5 \cdot 10^{-17} \tag{26}$$

Consequently, the through-membrane water mass flux due to EOD ($\dot{m}_{w,EOD}$) is calculated as a function of the local current density.

$$\dot{m}_{w,EOD} = n_d \cdot \frac{i}{F} M_w \tag{27}$$

Counteracting the EOD, a concentration gradient typically forms between the electrodes due to water production at the cathode catalyst layer and depletion at the anode catalyst layer. This gradient drives a diffusive flux through the membrane void space. As water accumulation is generally higher at the cathode, particularly at elevated current densities, this diffusion is typically anode-oriented (negative direction), hence termed back diffusion. The diffusive water mass flux ($\dot{m}_{w,BD}$) is modeled using Fick's law, as in Eq. (28).

$$\dot{m}_{w,BD} = -D_{w,mem}\nabla c_w M_W \approx -D_{w,mem}\left(\frac{c_{w,c} - c_{w,a}}{\delta_{mem}}\right) M_W \tag{28}$$

In particular, $D_{w,mem}$ is the diffusivity of dissolved water in the membrane, and c_w is the molar concentration of water at the electrode interfaces.

To integrate this effects in the model the above-mentioned fluxes are converted into volumetric source terms (Eqs. (29), (30) applied to the computational cells of the catalyst layers. The net flux is divided by the respective catalyst layer thickness (δ_{CL}) to ensure dimensional consistency, resulting in a sink/source term at the anode (water removal/injection) and a sink/source term at the cathode ensuring global mass conservation.

$$S_{w,a} = -\frac{(\dot{m}_{w,EOD} + \dot{m}_{w,BD})}{\delta^a_{CL}} \tag{29}$$

$$S_{w,c} = +\frac{(\dot{m}_{w,EOD} + \dot{m}_{w,BD})}{\delta^c_{CL}} \tag{30}$$

Fig. 1 visualizes this approach: the superposition of $\dot{m}_{w,EOD}$ and $\dot{m}_{w,BD}$ determines the net water transport, which is then spatially resolved as volumetric sources within the anode and cathode domains.

3. Description of experimental setup and the computational model

To date the experimental and numerical research on PEMFCs experiences the lack of standardized testing protocols for single-cell hardware setup. Consequently, each hardware configuration typically features unique flow field and cell designs, which significantly influence the specific test results and invalidate the generalization of the obtained results. To address this issue, the authors of [2,3] and the OEMs that partnered the study conducted an experimental campaign aimed at developing reference test hardware setups for harmonized single PEMFC testing protocols for automotive applications. The experimental setup described in the following is sourced from [2] and is here described as part of the creation of the numerical model of the two PEMFC designs (Single-Serpentine Hardware, SSHW and Zero-Gradient Cell, ZGC). The objective of these designs was to ensure consistent and reproducible testing of MEAs across different laboratories and for simulation studies, and the details are provided to contextualize the computational methodology and the imposed boundary conditions.

The SSHW configuration adopts a single-serpentine channel geometry, replicating the flow fields commonly found in commercial fuel cells tailored for laboratory-scale experiments, with an active area equal to 25 cm^2. The SSHW cell is used as a reference baseline PEMFC design.

The ZGC configuration employs a parallel flow channel layout, designed to maximize the uniformity of the membrane's operational status (i.e., humidification, temperature distribution, etc.). The main features of the configuration are summarized as:

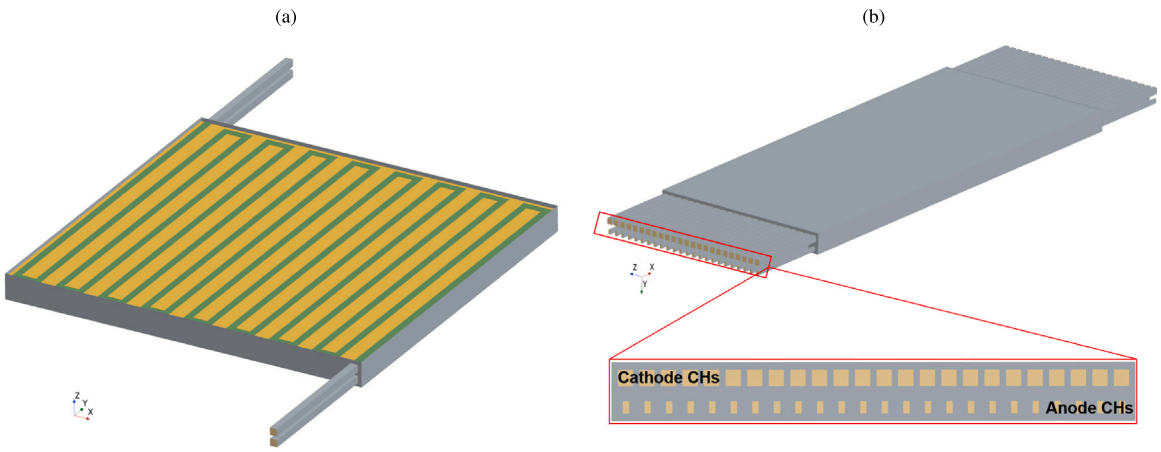

Fig. 2. Computational domains of the simulated cells: (a) Single-Serpentine testing Hardware (SSHW), (b) Zero-Gradient Cell (ZGC).

- Active area equal to 10 cm^2.
- Straight and parallel gas channels representative of typical automotive PEMFC flow fields.
- Constant gas flow rates of humidified reactants (air and H_2).
- Stable operation at a current density of 4.0 A cm^{-2}, characterized by:
  - Laminar flow regime (Reynolds number, Re < 1000).
  - Reactant pressure drop across the active area (anode and cathode) below 10.0 kPa.
  - Temperature variation within ±1.0 °C across the active area.

The aim is to ensure a quasi-uniform operating conditions across the entire MEA active area, thus minimizing the influence of specific hardware features on the experimental results. Achieving this uniformity requires a careful control of flow velocity, pressure, temperature, and species concentration. Although these tests are conducted at the single-cell level, the operating conditions are representative of those in commercial fuel cell systems, with the exception of the high stoichiometry factors (SR_a = 8, SR_c = 10). In addition, accurate control over the compression of the tested MEA is maintained throughout performance and durability tests.

The two described geometries were utilized to validate the computational methodology and demonstrate the insights that can be gained through detailed CFD simulations. The numerical domain of the SSHW cell is reported in Fig. 2(a). The cell is symmetric with respect to the MEA plane, with identical anodic and cathodic parts. To ensure fully developed flows within the domain of interest, 5 mm extrusions were added at inlet and outlet boundaries. For the SSHW model, a hexahedral finite-volume mesh was employed, consisting of 2.16 million cells encompassing the MEA, the porous parts (GDLs and CLS), the two reactant channels, and the two bipolar plates (BPs). This corresponds to a mesh density of 86,400 cells/cm^2, which is consistent with the recommendations and findings reported in Edwards et al. [21]. The numerical domain of the ZGC is shown in Fig. 2(b). The active area is 10 cm^2 (20 mm x 50 mm), and the cell is not symmetric with respect to the MEA plane, with differently sized anodic and cathodic channels. Identical 5 mm extrusions were added at inlet and outlet boundaries to ensure fully developed flows within the domain of interest. For the ZGC model, a hexahedral finite-volume mesh was employed, consisting of approximately 4.55 million cells. The resulting mesh density of 455,000 cells/cm^2 is due to the smaller channel dimensions of the ZGC configuration, necessitating a higher mesh resolution. More details on the characteristic geometry of the cell are shown in Table 2.

For what concerns the MEA of the two models, in [22] two specific MEAs are described. In this study, the so called *MEA 2* is used for validation, having an 8 μm-thick membrane, while CLs and GDLs are 5 μm and 235 μm thick, respectively. The platinum loading is differentiated between anode and cathode, with 0.1 mg cm^{-2} being used in the ACL and 0.4 mg cm^{-2} in the CCL. It is important to note that for both models the MEA has the same grid resolution in the through-plane direction, and mesh details are visible in Fig. 3.

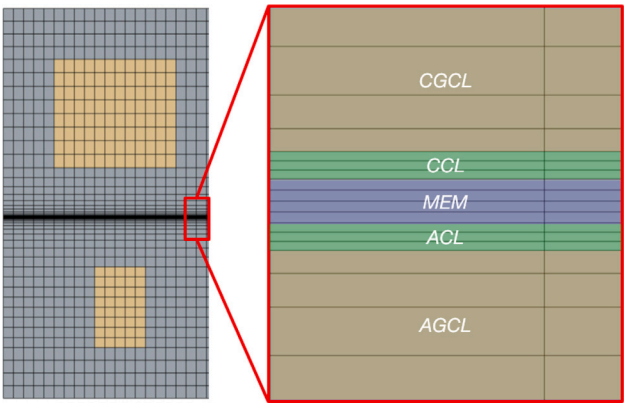

Fig. 3. Details of the MEA mesh used for the SSHW and ZGC models.

The operating conditions used for the models validation are reported in Table 3. Both cells share the same boundary conditions except for the stoichiometric ratios at the anode and cathode, defined as the ratio between the anodic/cathodic inlet flow rate over the electrochemical consumption rate of hydrogen or oxygen, respectively. In particular, the ZGC operates with very high stoichiometric factors to achieve the so-called *zero-gradient* conditions, albeit these far from the conditions of practical interest due to the associated power demand on the air compressor, lowering the fuel cell system efficiency [23]. On the other hand, the SSHW is tested with very low stoichiometric factors both at the anode and the cathode. Finally, Table A.5 reports the main material properties used in the 3D-CFD models of the SSHW and ZGC.

4. Results

4.1. Electrical characterization

The simulated polarization curves for the SSHW and ZGC cases are shown in Fig. 4(a). In the simulations, the voltage range for the ZGC design spans from 0.2 to 0.9 V with a resolution of 0.1 V, whereas for the SSHW configuration the voltage range extends from 0.4 to 0.9 V. The current–voltage relationship is accurately reproduced in both cases without cell-specific model calibration. The simulation results agree

Table 2
Geometrical details of the SSHW and ZGC.

Cell		Channel height [mm]	Channel width [mm]	Pitch [mm]
SSHW	Anode	1.0	1.0	2.0
	Cathode	1.0	1.0	2.0
ZGC	Anode	0.25	0.25	0.84
	Cathode	0.40	0.60	0.84

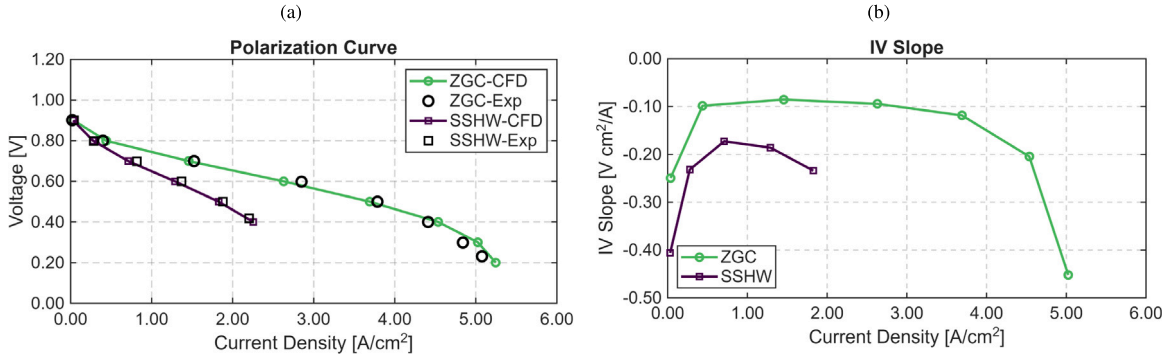

Fig. 4. Electrical Characteristics of the cells: (a) polarization curves, (b) IV slopes for the SSHW and ZGC.

Table 3
Boundary conditions for the SSHW and ZGC.

Fluid	Parameter	SSHW	ZGC
Hydrogen	Inlet temperature [K]	353.15	353.15
	Inlet relative humidity [–]	100	100
	Outlet pressure [kPa]	250	250
	Inlet stoichiometry [–]	1.3	8
Air	Inlet temperature [K]	353.15	353.15
	Inlet relative humidity [–]	100	100
	Outlet pressure [kPa]	230	230
	Inlet stoichiometry [–]	1.5	10

with the experimental data from [2] in entire simulated voltage range, although there is a minor overestimation of the current density at the lowest voltages for the ZGC model.

As in [2], in addition to the polarization curves the corresponding IV slopes $\frac{dV}{di}$ are presented in Fig. 4. The slopes of the polarization curves provide a more accurate visualization of the three operating regions, namely (i) the electrochemical kinetics region, (ii) the ohmic region, and (iii) the mass transport limitation region. Focusing on the SSHW, only two regions can be distinguished: the electrochemical kinetics and the mass transport limited region, with positive and negative slopes, respectively. The absence of a constant IV slope region indicates a direct transition to the mass transport limitation region, thus bypassing the ohmic one. In particular, the mass transport limitation region appears after 1.0 A/cm^2, where the IV slope becomes negative. The transition to this region at relatively low currents is motivated by the very low stoichiometric factors at which the cell operates ($SR_a = 1.3$, $SR_c = 1.5$). By examining the polarization behavior of the ZGC configuration, it is evident that the onset of the mass transport limited region emerges at higher current densities than for the SSHW cell. Specifically, the ZGC exhibits a nearly constant IV slope over a wide operating range, indicative of predominant operation within the ohmic region. This behavior reflects efficient electron and proton transport, as well as the absence of significant mass transport limitations under high flow rates ($SR_a = 8.0$, $SR_c = 10.0$). At higher current densities, however, the IV slope gradually decreases, indicating the transition to the mass transport limitation region. This transition marks the onset of oxygen and hydrogen diffusion limitations at the CLs.

The good agreement between experiments and simulations for both cells implies the robustness of the numerical framework, demonstrating its reliability across a range of electric potentials and diversified geometries. Examining the two polarization curves and their slopes, it is clear that the SSHW cell exhibits overpotentials higher than those of the ZGC. The reasons for this discrepancy will be discussed and analyzed using CFD results in the next paragraphs.

4.2. Thermal characterization

In the referenced experimental study [2,3], temperature measurements were conducted at the inlet, middle, and outlet sections of the active area for the ZGC, on both the anode and cathode sides, approximately 3 mm from the active region. These measurements were used to monitor the mole fraction of water vapor, estimated using the ideal gas law, to verify uniform humidity conditions in the active area. The authors reported temperature variations below ±1 °C, corresponding to less than a 1% variation in the water vapor mole fraction, thereby confirming a nearly uniform humidity distribution during operation. In the present work, the simulations provide complementary insight by enabling the evaluation of local temperature distributions not only on the anode and cathode sides but also within the membrane itself, a measurement that is experimentally challenging to obtain. Fig. 5 presents the simulated temperature values for the ZGC configuration as registered by probe lines at inlet/center/outlet cell sections, showing that the temperature variation remains below ±1 °C on both gas sides, in agreement with the experimental findings. Importantly, the CFD results also reveal that the temperature variations within the membrane (Fig. 5(d)) are similarly limited to within ±1 °C, both along the through-plane (z) direction and between the virtual probe locations. Only at very high current densities does a slightly larger temperature difference appear.

Overall, these findings demonstrate that the CFD model not only reproduces the experimental temperature uniformity but also extends the analysis by providing spatially resolved temperature information within the membrane, thus offering a more complete understanding of the coupled heat and mass transport phenomena in PEMFC operation.

4.3. Flow characteristics

In Section 3, it was emphasized that, in addition to temperature variations, other parameters such as the Reynolds number and the pressure drop across the active area must also be carefully controlled. The Reynolds number at anode and cathode outlets has been measured

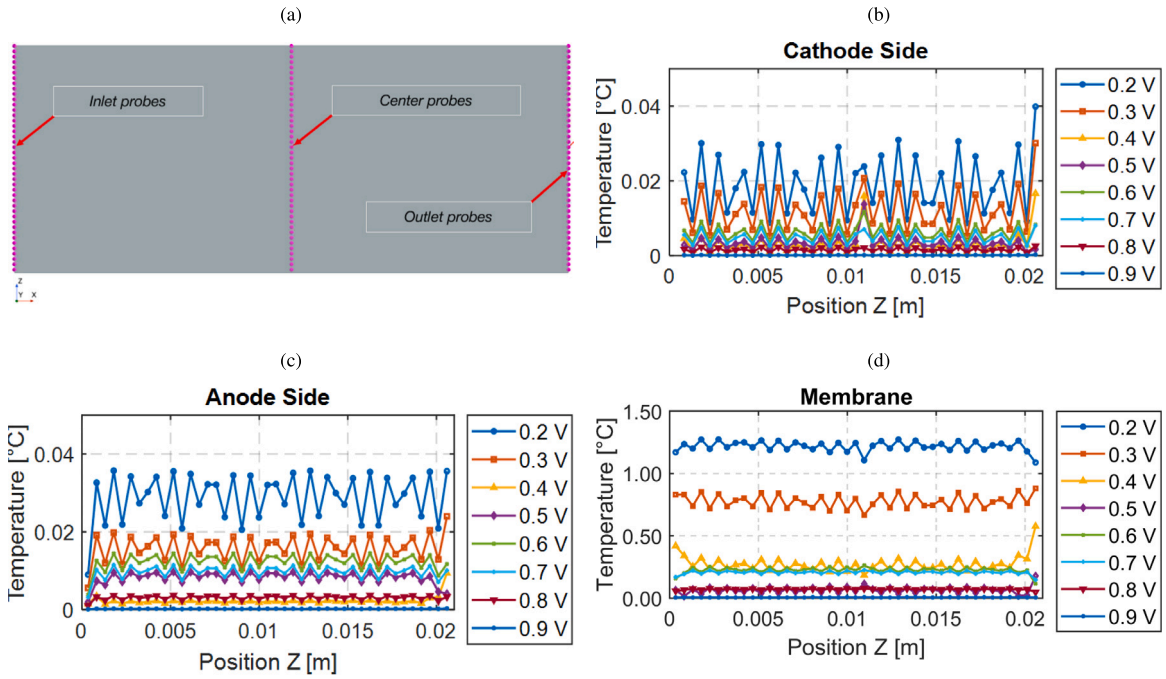

Fig. 5. Temperature difference between the maximum and the minimum along the z direction for the ZGC.: (a) probes position view from the top of the cell, (b) temperature difference at cathode side, (c) temperature difference at anode side, (d) Temperature difference on the membrane.

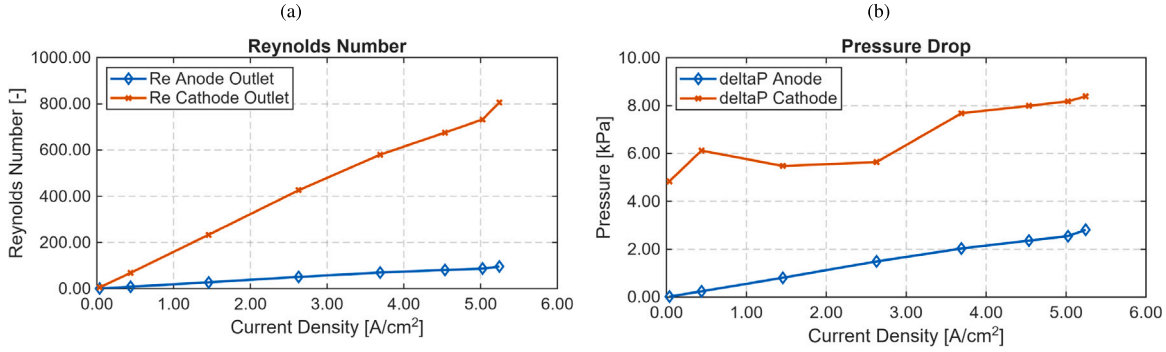

Fig. 6. Simulated Reynolds number (a) and pressure drop (b) for the ZGC.

only for the ZGC, and it is illustrated in Fig. 6(a), calculated using Eq. (31) and (32) where the channel-specific hydraulic diameter is used as a length scale, as well as the specific fluid properties. As seen in Fig. 6(a), the Reynolds numbers for both the anode and cathode remain below 1000, confirming a laminar flow regime in both channels. Maintaining a laminar flow regime within the fuel cell is crucial as it promotes uniform flow distribution across the porous media, resulting in minimum pressure losses between the inlet and outlet. This is confirmed by Fig. 6(b), which shows that the pressure drop consistently remains below 10 kPa for both channels.

$$Re_{anode} = \frac{\rho \cdot u \cdot D_{h,anode}}{\mu} \quad \text{where} \quad D_{h,anode} = \frac{4 \cdot A}{P} = 0.25 \cdot 10^{-3} m \tag{31}$$

$$Re_{cathode} = \frac{\rho \cdot u \cdot D_{h,cathode}}{\mu} \quad \text{where} \quad D_{h,cathode} = \frac{4 \cdot A}{P} = 0.48 \cdot 10^{-3} m \tag{32}$$

4.4. Spatial distribution analysis

After the models' validation against the available experimental acquisitions, the analysis moves to experimentally inaccessible quantities of high relevance to explain the different operation of the two cells. As illustrated in Fig. 7(a), the CCL in the SSHW cell is subject to an oxygen deficiency immediately after the initial cell segment at 0.4 V and a current density of 2.25 A/cm^2. This oxygen starvation is evident not only in the catalyst layer, but also within the channels, as visible in Fig. 8(a), suggesting that the SSHW limitations arise from an actual deficiency in reactant supply, combined with the low reactant diffusion rate. The entity of oxygen starvation, caused by the low stoichiometric factor, leads to significant mass transport losses, ultimately resulting in the high overpotentials observed for the SSHW. Moving to the ZGC, the CCL shows a relatively uniform oxygen distribution across the catalyst layer at 0.4 V and a current density of 4.54 A/cm^2 (Fig. 7(b)), although a moderate oxygen shortage is visible approaching the cell outlet. This indicates that the supply rate of reactant at the active sites is constrained by the limited diffusivity and permeability of the porous media, despite the high stoichiometric factor. This phenomenon is further confirmed by Fig. 8(b), where a high oxygen mole fraction is observed within the gas channel, consistent with the high stoichiometric factor utilized, but a much smaller fraction effectively diffuses through the porous layers toward the catalyst sites.

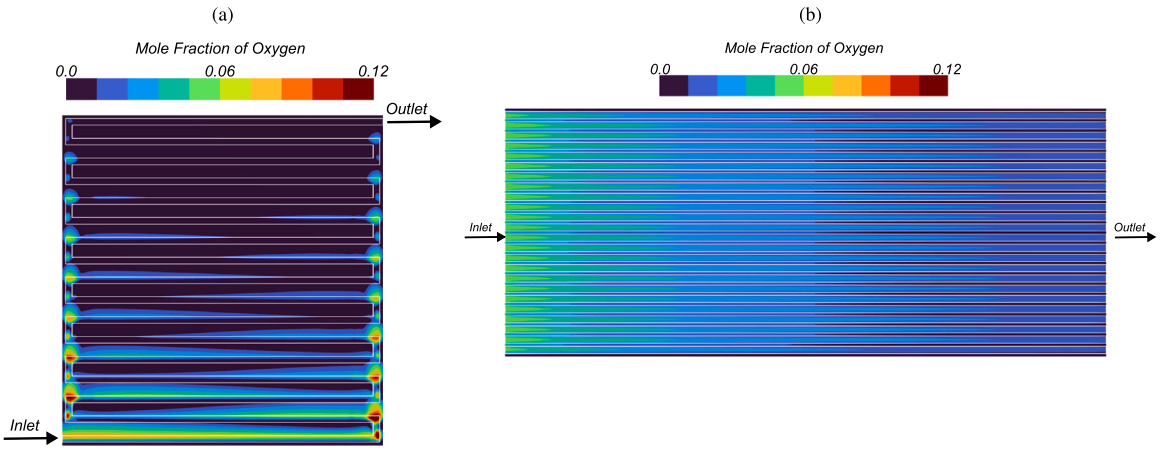

Fig. 7. Spatial distribution of the mole fraction of oxygen at 0.4 V: (a) CCL of the SSHW (2.25 A/cm^2), (b) CCL of the ZGC (4.54 A/cm^2).

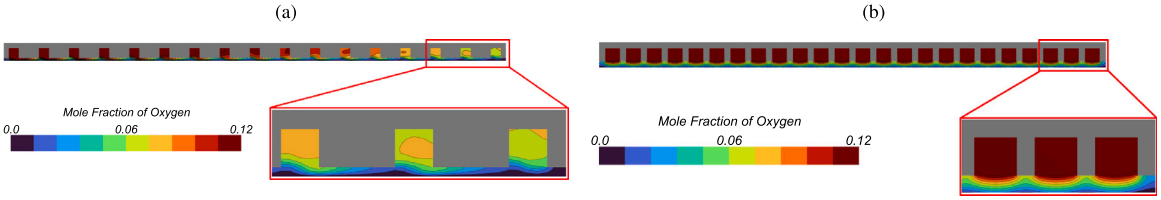

Fig. 8. Spatial distribution of the mole fraction of oxygen at 0.4 V: (a) cathode channels of the SSHW (2.25 A/cm^2), (b) cathode channels of the ZGC (4.54 A/cm^2).

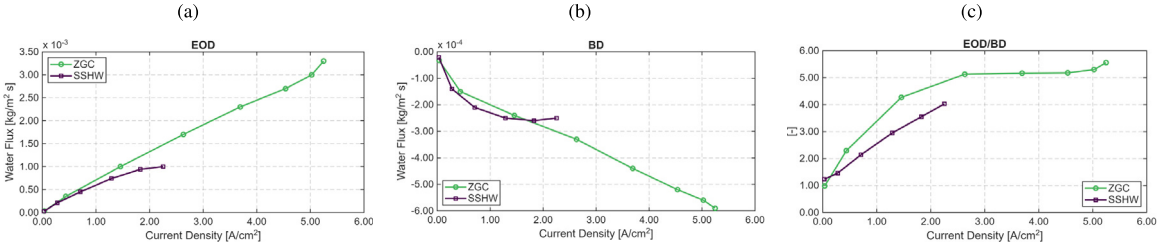

Fig. 9. Water mass flux analysis: (a) water mass flux due to electro-osmotic drag (EOD), (b) water mass flux due to back-diffusion (BD), (c) EOD over BD ratio.

4.5. Water flux analysis

A key aspect of the polymeric membrane of PEMFCs is the need to remain uniformly humidified to maximize the ionic conductivity. Given its importance, a sub-model that accurately predicts the water transport due to membrane fluxes and phase transition is in high demand to enable the spatially resolved prediction of the cell's performance. This contribution relevantly extends the general understanding of the differences between SSHW and ZGC, considering that none of the discussed water fluxes has been experimentally measured.

Fig. 9 reports the results of the water mass flux across the membrane from EOD and BD, $\dot{m}_{EOD}$ and $\dot{m}_{BD}$ respectively. Fluxes (i.e., per-unit-surface flow rates) are preferred over integral values to facilitate the results generalization, and the convention of positive flux for cathode-oriented transport is chosen. The relative contributions of EOD and BD is evaluated through the EOD/BD ratio, defined as the ratio of the EOD mass flux to the absolute value of the BD mass flux [6], as shown in Eq. (33), where values higher than unity express a dominance of the EOD transport mechanism over the BD one.

$$EOD/BD = \frac{\dot{m}_{EOD}}{|\dot{m}_{BD}|} \tag{33}$$

As expected, for both cells the EOD flux ($\dot{m}_{EOD}$) shows an almost linear increasing trend as a function of the current density, whereas the BD flux ($\dot{m}_{BD}$) is negative (i.e., anode-directed) and characterized by a different trend based on the mixture of the reactants in contact with the membrane. It is underlined that both SSHW and ZGC models share the same membrane thickness and dissolved water diffusivity, hence the different $|\dot{m}_{BD}|$ is to be attributed to differences in the concentration gradients of water at ACL and CCL. In particular, in Fig. 9(c), the ratio between EOD and BD flux is represented, indicating that the EOD flux is always higher than the BD one (EOD/BD ratio higher than unity). This is in line with the numerical analysis in [6] on a laboratory small-scale straight channel PEMFC simulated at high/low stoichiometry. It is evident that for the ZGC, the EOD water transport mechanism is significantly stronger compared to that observed in the SSHW configuration. This is mainly attributed to the higher current density produced by the ZGC, promoting higher $\dot{m}_{EOD}$. Consequently, the EOD/BD ratio is also generally higher in the ZGC. The root cause for the higher current densities achievable with the ZGC is the operation at higher stoichiometric factors, which, combined with a larger cross-sectional area (parallel channels) and minimum pressure losses (short inlet–outlet distance), allows for a uniform and abundant supply rate of reactants over the active surface.

The dominance of $\dot{m}_{EOD}$ over $\dot{m}_{BD}$ causes the anodic dehydration and the cathodic super-saturation reported in Fig. 10, which is generally observed for both cells. In particular, the SSHW design suffers a critical dehydration even at moderate current density, because of the

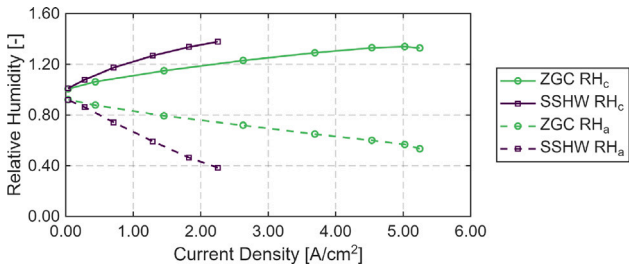

Fig. 10. Volume average relative humidity at ACL and CCL for the SSHW and ZGC.

limitation in the water vapor supply rate in comparison to the ZGC design. In addition to the volume averaged data shown in Fig. 10, the spatial distribution of RH is shown in Fig. 11 at the CCL, and in Fig. 12 at the ACL. For the CCL, humidification issues are absent because water is generated by both the ORR reaction and transported by the strong EOD mechanism. The situation is different at the ACL: Fig. 12(a) shows severe dehydration in the ACL of the SSHW cell at 2.25 A/cm^2, with some areas experiencing relative humidity as low as RH = 0.1. In contrast, the ACL for the ZGC exhibits a better and more uniform spatial distribution of relative humidity at 4.54 A/cm^2, maintaining a consistently low, albeit uniform, humidity level throughout the entire surface.

Moving to the analysis of the membrane status, the membrane water content is related to the RH levels in the ACL and CCL, as expressed by Eq. (24). Fig. 13(a) illustrates the volume averaged membrane water content and Fig. 13(b) the volume average electrical conductivity. For the SSHW configuration, it is evident that significant anode dehydration results in a critically low membrane water content. This, in turn, leads to low electrical conductivity, which, combined with low stoichiometric factors, leads the SSHW cell to have a higher ohmic overpotential than the ZGC.

Fig. 14(a) presents the spatial distribution of the membrane water content for the SSHW configuration. A generally low and non-uniform water content is observed, with locally elevated values near the outlet section. Two key aspects emerge from this distribution:

- Most of the membrane operates under sub-optimal hydration, which can adversely affect ionic conductivity.
- The regions exhibiting an optimal water content correspond to areas with little or no electrochemical activity due to reactant depletion (e.g., close to the channel outlet), as shown in Fig. 7(a), suggesting that proper membrane hydration is achieved primarily in non-reactive zones.

In contrast, the ZGC configuration (Fig. 14(b)) displays a generally higher and more uniform membrane water content, in line with the temperature field reported in Fig. 5. This improved uniformity is favored by the parallel channels layout, which promotes an even distribution of reactants and facilitates the water removal over the membrane. Such a distribution prevents local dehydration and ensures a more uniform hydration throughout the active area. This balanced membrane hydration underscores the effectiveness of ZGC hardware in establishing optimal conditions for the PEMFC testing. These numerical findings complement the experimental results reported by Bednarek and Tsotridis [2], where no optical diagnostics were available to directly assess the MEA water distribution.

4.6. Overpotentials analysis

Finally, a loss-specific analysis of the overpotentials across the entire range of operating voltages is presented in Fig. 15, based on the simulation results. Fig. 15(a) shows the ohmic losses, which are mainly due to the charge transport resistance of the electrolyte, electrode materials, and interconnections within the cell, and they are linearly dependent on the current density (Ohm's law). At higher currents resistive losses increase, significantly contributing to the overall cell overpotential. However, the SSHW cell experiences higher losses compared to the ZGC, even when compared at the same current density. This is motivated by the available contact surface between BPs and GDLs, which equals 7.9 cm^2 in the SSHW and 5.2 cm^2 in ZGC (per cell side): however, when this is rationalized over the entire active area for the two cells (25/10 cm^2 for the SSHW/ZGC), this results in the use of 32% of the available area for charge transport in the SSHW, and in 52% for the ZGC. Therefore, the ZGC minimizes the ohmic overpotential thanks to a larger pathway for facilitated charge transport, a decisive design factor that combines with the operation at higher ionic conductivity (see Fig. 13(b)) to minimize the ohmic overpotential.

Regarding the mass transport losses, Fig. 15(b), these become more relevant at high current density as the demand for reactants supply rate increases, and the limited diffusion becomes insufficient to support the conversion rate at the electrodes. Consequently, this increases the concentration gradients and reduces the electrochemical reaction rates. The SSHW cell shows higher mass transport losses with respect to the ZGC as a result of (i) the low stoichiometric factor and of (ii) the single-channel configuration that precludes a uniform reactants supply rate over the entire surface area.

Finally, Fig. 15(c) presents the activation losses. These losses are typically the largest overpotential in PEMFCs, and they origin due to the slow kinetics of the oxygen reduction reaction (ORR) at CCL. This overpotential dominates because the slow reaction rate of the ORR leads to a significant charge transfer overpotential. This is a known challenge in low-temperature electrochemical systems, despite the CCL-biased catalyst loading to mitigate this effect (0.1 mg/cm^2 at ACL, 0.4 mg/cm^2 at CCL). These considerations are in line and relevantly integrate the EIS-derived conclusions in [2], providing quantitative interpretations to the loss analysis methodology.

4.7. Discussion and limitations

The ZGC configuration significantly outperforms the SSHW setup by reducing both ohmic and mass transport losses, emphasizing its superior design and efficiency. This was a clear experimental outcome, and it is used to validate the two largely different PEMFC configurations (SSHW and ZGC) simulated in this study. The study quantitatively indicates the specific limitations and peculiarities of each cell via multidimensional, non-isothermal and multiphase models, relying on hypotheses that are indicated as study limitations and areas of simulation improvement:

- Steady-state analysis: the model is explicitly defined under steady-state conditions. This represents a major limitation, as it cannot capture transient phenomena such as startup, shutdown, or load variations.
- MMP model: the adoption of the Mixture Multiphase (MMP) model implies inherent simplifications. This approach assumes that the phases are fully miscible and in local thermodynamic equilibrium and that the continuous phase (gas) is largely dominant over the dispersed one (liquid), solving a single set of conservation equations for the mixture. More advanced approaches, such as a full Eulerian–Eulerian framework, could provide a more detailed representation of interphase interactions and velocity slip between the gas and liquid phases.
- Macro-homogeneous porous media: GDLs and CLs are modeled as homogeneous porous media, which inherently averages the complex microstructure of carbon fibers, pores, and catalyst agglomerates. As a result, the model cannot resolve pore-scale phenomena, such as local liquid water pathways or gas transport limitations within the GDL.

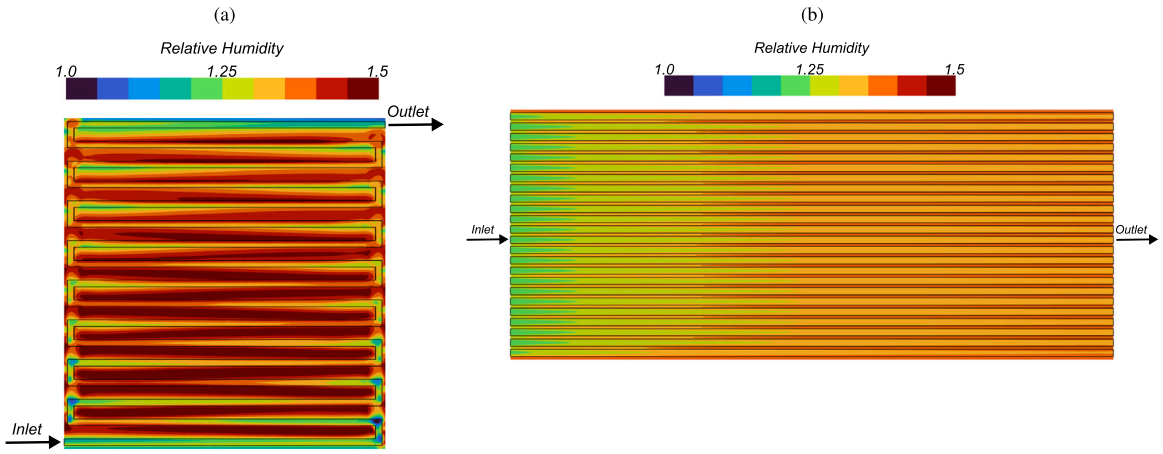

Fig. 11. Spatial distribution of RH at 0.4 V at CCL for the SSHW (left) and ZGC (right) cell: (a) ACL of the SSHW (2.25 A/cm^2), (b) ACL of the ZGC (4.54 A/cm^2).

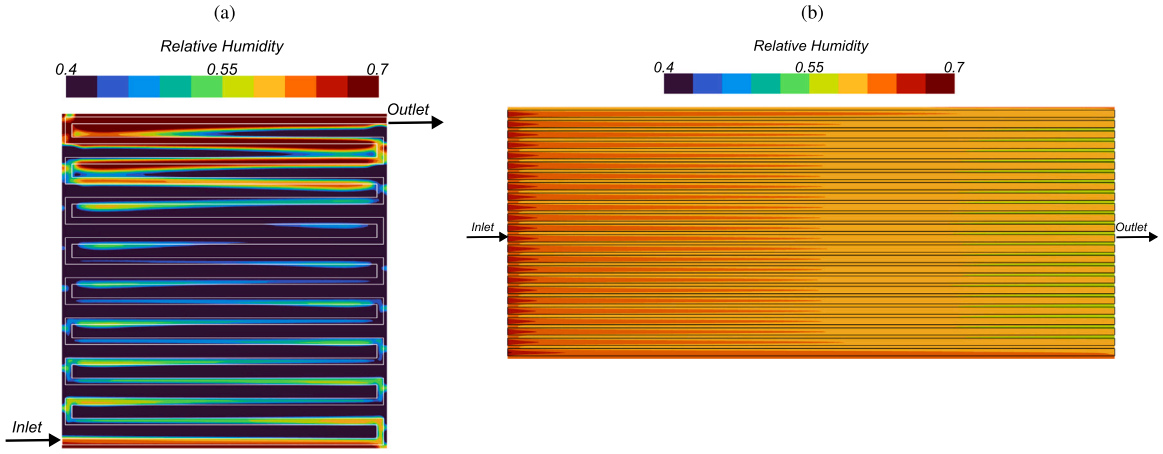

Fig. 12. Spatial distribution of RH at 0.4 V at ACL for the SSHW (left) and ZGC (right) cell: (a) ACL of the SSHW (2.25 A/cm^2), (b) ACL of the ZGC (4.54 A/cm^2).

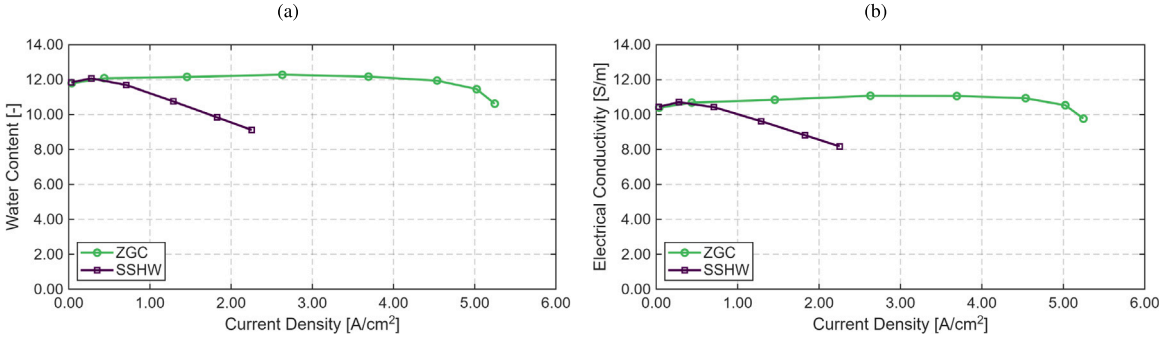

Fig. 13. Volume averaged membrane conditions: (a) volume average membrane water content, (b) volume average membrane ionic conductivity.

- Finite-rate sorption kinetics: the rates of water absorption and desorption at the membrane boundaries are not rate-limiting processes, a simplification that does not fully reflect reality [24]. This assumption may influence the predicted water content distribution; consequently, the integration of finite-rate sorption kinetics into the simulation methodology is a subject of ongoing investigation. Furthermore, the membrane is modeled as impermeable to the bulk gas mixture, allowing only the transport of dissolved water and protons. While this formulation neglects gas crossover (e.g., hydrogen permeation from anode to cathode) and the associated minor voltage losses, this specific phenomenon has been extensively addressed in a recent work [6].

5. Conclusions

The presented simulation study provides a comprehensive understanding of the fluidic, thermal, and electrochemical differences of the SSHW and ZGC hardware configurations through advanced 3D-CFD models. The experimental campaign in [2] demonstrated significant differences between two investigated designs (SSHW and ZGC), albeit being inherently limited to measurable quantities (e.g., current, voltage, pressure drop, temperature, and EIS-derived overpotentials) with no information on the spatial distributions of species and membrane status.

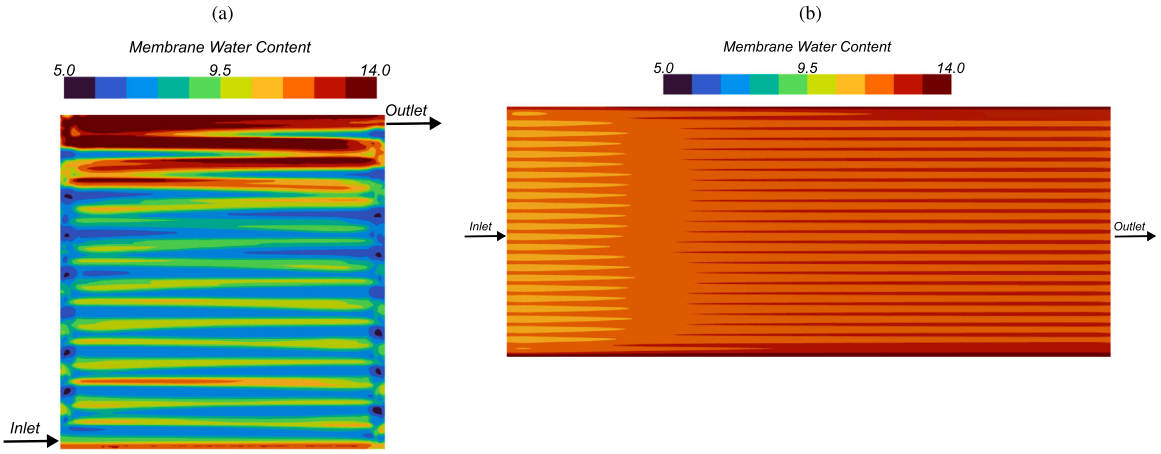

Fig. 14. Spatial distribution of the membrane water content at 0.4 V: (a) membrane of the SSHW (2.25 A/cm^2), (b) membrane of the ZGC (4.54 A/cm^2).

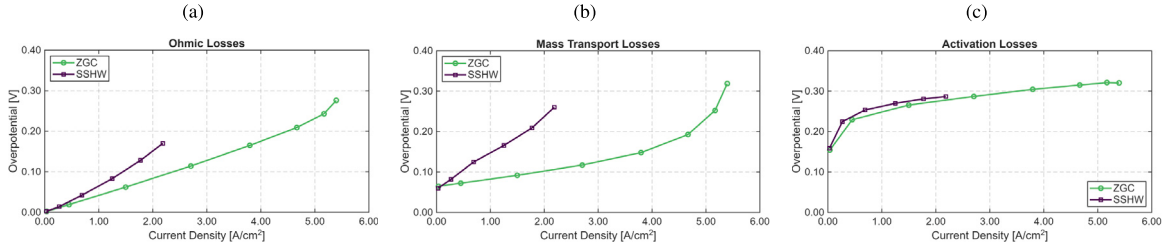

Fig. 15. Overpotential comparison between SSHW and ZGC: (a) ohmic losses. (b) mass transport losses, (c) activation losses.

In this work, the presented 3D-CFD models for the SSHW and ZGC included an in-house implemented sub-model for membrane water flux modeling, and the simulation results were validated based on the following outcomes:

- The experimental voltage–current characteristics (polarization curves) and their first derivatives for both SSHW and ZGC designs were accurately reproduced by simulation results, validating the robustness of the modeling approach and confirming its ability to represent largely different PEMFC configurations and low/high flow rates (SR_a = 1.3, SR_c = 1.5 for the SSHW cell, SR_a = 8, SR_c = 10 for the ZGC).
- The experimental–numerical correlation was further extended to pressure drop and temperature spatial measurements (only available for ZGC).
- The compared SSHW/ZGC overpotential analysis has confirmed the EIS-derived outcomes from [2], integrating them with the indication that the root causes for ohmic loss reduction in the ZGC are (i) the larger fraction of the contact area between BPs and GDLs with respect to the entire active surface and (ii) the higher membrane water content and ionic conductivity. Mass transport losses are also lower for the ZGC due to the higher stoichiometric factors, whereas activation losses are almost identical for the two cells, as expected. The complex flow/energy/current interplay at the basis of the operation of each of the two tested cells is correctly reproduced by the presented 3D-CFD models, thus proving a solid physical soundness and a good geometry-independence quality.

Furthermore, the simulation results were used to analyze aspects not accessible by the experiments, expanding the understanding of the SSHW and ZGC operation in terms of:

- The membrane water flux analysis revealed that in both configurations the electro-osmotic drag flux consistently exceeds the back-diffusion one, causing anode dehydration. In this situation, the SSHW cell operated under a low stoichiometry undergoes a relevant anode dehydration, hence undermining the membrane water content and ionic conductivity under moderate current density. Conversely, the ZGC configuration mitigated the anode dehydration thanks to its higher stoichiometry, demonstrating a more uniform water management and a higher membrane water content and ionic conductivity under high current density.
- The electro-osmotic drag emerged as the dominant water transport mechanism across the membrane for both the SSHW and ZGC. The simulations also demonstrated that even at very high stoichiometric factors (SR_a = 8, SR_c = 10), a zero-gradient condition is not achieved. This is due to the limited diffusivity associated with the GDL porosity and the accumulation of water, leading to non-uniform gas distribution. Achieving homogeneous conditions was therefore challenging not only for reactants but also for temperature distribution across the membrane, particularly at low voltages where current densities are high.

This numerical study presented a multiphysics, non-isothermal and multi-phase model for the simulation of PEMFC, with an in-house implemented water transport sub-model which allowed quantitative analyses of the fluxes through the polymeric membrane. After an initial validation with the available experimental data, the study provides a deeper understanding of the physical mechanisms at the basis of the performance differences between the SSHW and ZGC configurations. The results highlight the influence of both the hardware design and the flow rate conditions on local hydration and mass transport limitations, and it demonstrates the potential of detailed multiphysics modeling to complement experimental campaigns by providing additional quantitative insights.

Table 4
Nomenclature.

Symbol	Description	Unit
Latin Symbols		
a	Water activity	[–]
A	Area	[m^2]
A_s	Specific active surface area	[m^{-1}]
c	Molar concentration	[kmol m^{-3}]
c_p	Specific heat capacity	[J kg^{-1} K^{-1}]
D	Diffusivity	[m^2 s^{-1}]
D_h	Hydraulic diameter	[m]
EW	Equivalent weight of ionomer	[kg $kmol^{-1}$]
f	Mass fraction of platinum on carbon support	[–]
F	Faraday's constant	[C $kmol^{-1}$]
H_{lat}	Latent heat of vaporization	[J kg^{-1}]
i	Superficial current density	[A m^{-2}]
j	Volumetric current density	[A m^{-3}]
j_0	Exchange current density	[A m^{-3}]
k	Thermal conductivity	[W m^{-1} K^{-1}]
K	Absolute permeability	[m^2]
k_C	Condensation rate constant	[s^{-1}]
k_E	Evaporation rate constant	[Pa^{-1} s^{-1}]
M	Molar mass	[kg $kmol^{-1}$]
$\dot{m}$	Mass flux/Phase change rate	[kg m^{-2} s^{-1}]
m_{Pt}	Platinum loading	[kg m^{-2}]
n_d	Electro-osmotic drag coefficient	[H_2O/H^+]
P	Perimeter	[m]
p	Pressure	[Pa]
Q	Volumetric heat source due to phase change	[W m^{-3}]
R	Universal gas constant	[J $kmol^{-1}$ K^{-1}]
Re	Reynolds number	[–]
$\vec{S}_{cap}$	Momentum source term due to capillary forces	[kg m^{-2} s^{-2}]
S	Entropy	[J K^{-1}]
S_k	Volumetric species source term	[kg m^{-3} s^{-1}]
S_m	Volumetric mass source term	[kg m^{-3} s^{-1}]
S_T	Volumetric heat source term	[W m^{-3}]
S_Φ	Volumetric potential source term	[A m^{-3}]
SR	Stoichiometric Ratio	[–]
$\vec{S}_V$	Porous resistance momentum source	[kg m^{-2} s^{-2}]
T	Temperature	[K]
$\vec{V}_{mix}$	Superficial (Darcy) velocity	[m s^{-1}]
x	Mole fraction	[–]
Y	Mass fraction	[–]
z	Charge number	[–]
Greek Symbols		
α	Charge transfer coefficient	[–]
γ	Surface tension	[N m^{-1}]
δ	Thickness	[m]
ϵ	Porosity	[–]
ζ	Specific catalyst area parameter	[m^2 m^{-3}]
$\zeta_{im/C}$	Ionomer to carbon mass ratio	[–]
$\zeta_{Pt/C}$	Platinum to carbon mass ratio	[–]
η	Overpotential	[V]
θ	Contact angle	[deg]
κ	Effective permeability	[m^2]
λ_{mem}	Membrane water content	[–]
μ	Dynamic viscosity	[Pa s]
ρ	Density	[kg m^{-3}]
σ	Conductivity	[S m^{-1}]
τ	Tortuosity	[–]
Φ	Potential	[V]
χ	Volume fraction	[–]
Subscripts and Superscripts		
a, c	Anode, Cathode	
BD	Back Diffusion	
CL	Catalyst Layer	
e	Electrolyte (ionic phase)	
eff	Effective property	
EOD	Electro-osmotic drag	
g, l	Gas, Liquid phase	
GDL	Gas Diffusion Layer	
im	Ionomer	
mem	Membrane	
mix	Mixture	
Pt	Platinum	
Pt/C	Platinum Carbon	
ref	Reference value	
s	Solid (electronic phase)	
sat	Saturation	
w	Water	

(*continued on next page*)

(*continued*).

Nomenclature

See Table 4.

CRediT authorship contribution statement

Carmine Marra: Writing – review & editing, Writing – original draft, Software, Methodology, Investigation, Formal analysis, Data curation, Conceptualization. **Marcos López Juárez:** Writing – review & editing, Methodology, Investigation. **Giacomo Filippini:** Writing – original draft, Software, Methodology, Investigation. **Ricardo Novella:** Writing – review & editing, Project administration. **Stefano Fontanesi:** Writing – review & editing, Project administration. **Alessandro d'Adamo:** Writing – review & editing, Supervision, Project administration, Methodology, Funding acquisition, Conceptualization.

Declaration of competing interest

The authors declare the following financial interests/personal relationships which may be considered as potential competing interests: Carmine Marra reports financial support was provided by European Union. Alessandro d'Adamo reports financial support was provided by University of Modena and Reggio Emilia Department of Engineering Enzo Ferrari. If there are other authors, they declare that they have no known competing financial interests or personal relationships that could have appeared to influence the work reported in this paper.

Acknowledgments

Carmine Marra acknowledges the financial support provided by European Union, NextGenerationEU for PhD Scholarship funding at Dipartimento di Ingegneria "Enzo Ferrari" (Università degli Studi di Modena e Reggio Emilia), Italy, CUP: E93C23001710008, Corso: DOT1317193 - INGEGNERIA MECCANICA E DEL VEICOLO. Alessandro d'Adamo acknowledge the financial support provided by European Union, NextGenerationEU - National Sustainable Mobility Centre - MOST, Italy, CN00000023, Italian Ministry of University and Research, Spoke 12, Italy (CUP E93C22001070001).

Appendix

See Table A.5.

Table A.5
Material properties of the simulated cell.

Component	Property	Value	Unit
GDL	Porosity (ϵ_{GDL})	0.7	–
	Permeability	$\frac{\epsilon_{GDL}^3 (10\times10^{-6})^2}{16\times4.2(1-\epsilon_{GDL})^2}$ [25]	m^2
	Contact angle	110	deg

(*continued on next page*)

Table A.5 (*continued*).

Component	Property	Value	Unit
CL	Porosity	0.4	–
	Permeability	$\frac{\epsilon_{CL}^3(10\times10^{-6})^2}{16\times4.2(1-\epsilon_{CL})^2}$ [25]	m^2
	Contact angle	110	deg
	Ionomer Phase:		
	Density	2000	kg m^{-3}
	Ionic Conductivity	Eq. (23)	S m^{-1}
	Specific Heat	903	J kg^{-1} K^{-1}
	Thermal Conductivity	0.445	W m^{-1} K^{-1}
	Volume Fraction	Eq. (17)	–
	Pt/C Phase:		
	Density	2000	kg m^{-3}
	Electrical Conductivity	512 000	S m^{-1}
	Specific Heat	903	J kg^{-1} K^{-1}
	Thermal Conductivity	0.445	W m^{-1} K^{-1}
	Pt Loading Anode	0.1	mg cm^{-2}
	Pt Loading Cathode	0.4	mg cm^{-2}
	Volume Fraction	Eq. (16)	–
BP	Density	2250	kg m^{-3}
	Electrical Conductivity	512 000	S m^{-1}
	Specific Heat	707.68	J kg^{-1} K^{-1}
	Thermal Conductivity	24	W m^{-1} K^{-1}
Membrane	Density	2000	kg m^{-3}
	Ionic Conductivity	Eq. (23)	S m^{-1}
	Specific Heat	903	J kg^{-1} K^{-1}
	Thermal Conductivity	0.445	W m^{-1} K^{-1}

References

[1] P. IEA, Global Hydrogen Review 2024, Technical Report, IEA, Paris, 2024.

[2] T. Bednarek, G. Tsotridis, Assessment of the electrochemical characteristics of a Polymer Electrolyte Membrane in a reference single fuel cell testing hardware, J. Power Sources 473 (2020) 228319, http://dx.doi.org/10.1016/j.jpowsour.2020.228319.

[3] T. Bednarek, G. Tsotridis, Comparison of experimental data obtained using the reference and the single-serpentine proton exchange membrane single fuel cell testing hardware, Data Brief 31 (2020) 105945, http://dx.doi.org/10.1016/j.dib.2020.105945.

[4] M.M. Mench, Fuel Cell Engines, John Wiley & Sons, Nashville, TN, 2008.

[5] F. Barbir, PEM fuel cells, in: Sustainable world series, Academic Press, San Diego, CA, 2005.

[6] A. d'Adamo, L. Martoccia, F. Croci, C. Marra, CFD simulation of the effect of membrane thickness and reactants flow rate on water management in PEM fuel cells, Int. J. Heat Mass Transfer 249 (2025-10) 127207, http://dx.doi.org/10.1016/j.ijheatmasstransfer.2025.127207, URL: https://linkinghub.elsevier.com/retrieve/pii/S0017931025005460.

[7] L. Martoccia, C. Antetomaso, S. Merola, C. Marra, S. Breda, A. D'Adamo, Effects of cell design improvement on an automotive PEMFC system, in: WCX SAE World Congress Experience, 2025-04-01, pp. 2025–01–8549, http://dx.doi.org/10.4271/2025-01-8549, URL: https://saemobilus.sae.org/papers/effects-cell-design-improvement-automotive-pemfc-system-2025-01-8549.

[8] C.-Y. Wang, Fundamental models for fuel cell engineering, Chem. Rev. 104 (10) (2004) 4727–4766, http://dx.doi.org/10.1021/cr020718s, PMID: 15669167 URL: https://doi.org/10.1021/cr020718s.

[9] C. Marra, F. Croci, S. Fontanesi, F. Berni, A. D'Adamo, Capillary transport analysis in macro-homogeneous diffusion media of PEM fuel cells, in: WCX SAE World Congress Experience, SAE International, 2025, pp. 2025–01–8546, http://dx.doi.org/10.4271/2025-01-8546.

[10] A. d'Adamo, M. Haslinger, G. Corda, J. Höflinger, S. Fontanesi, T. Lauer, Modelling Methods and Validation Techniques for CFD Simulations of PEM Fuel Cells, Processes 9 (4) (2021) 688, http://dx.doi.org/10.3390/pr9040688.

[11] D.A.G. Bruggeman, Berechnung verschiedener physikalischer konstanten von heterogenen substanzen. I. Dielektrizitätskonstanten und leitfähigkeiten der mischkörper aus isotropen substanzen, Ann. Phys., Lpz. 416 (7) (1935) 636–664, http://dx.doi.org/10.1002/andp.19354160705.

[12] K. Jiao, X. Li, Water transport in polymer electrolyte membrane fuel cells, Prog. Energy Combust. Sci. 37 (3) (2011-06) 221–291, http://dx.doi.org/10.1016/j.pecs.2010.06.002, URL: https://linkinghub.elsevier.com/retrieve/pii/S0360128510000511.

[13] G. Corda, S. Fontanesi, A. d'Adamo, Methodology for PEMFC CFD simulation including the effect of porous parts compression, Int. J. Hydrog. Energy 47 (32) (2022) 14658–14673, http://dx.doi.org/10.1016/j.ijhydene.2022.02.201, URL: https://www.sciencedirect.com/science/article/pii/S0360319922008680.

[14] N. Khajeh-Hosseini-Dalasm, M. Fesanghary, K. Fushinobu, K. Okazaki, A study of the agglomerate catalyst layer for the cathode side of a proton exchange membrane fuel cell: Modeling and optimization, Electrochim. Acta 60 (2012) 55–65, http://dx.doi.org/10.1016/j.electacta.2011.10.099, URL: https://www.sciencedirect.com/science/article/pii/S0013468611016513.

[15] B. Xie, G. Zhang, J. Xuan, K. Jiao, Three-dimensional multi-phase model of PEM fuel cell coupled with improved agglomerate sub-model of catalyst layer, Energy Convers. Manage. 199 (2019) 112051, http://dx.doi.org/10.1016/j.enconman.2019.112051.

[16] M. Manninen, V. Taivassalo, V. Energy, S. Kallio, On the mixture model for multiphase flow, in: On the Mixture Model for Multiphase Flow, VTT, 1996, URL: https://api.semanticscholar.org/CorpusID:906342.

[17] J.-P. Kone, X. Zhang, Y. Yan, G. Hu, G. Ahmadi, Three-dimensional multiphase flow computational fluid dynamics models for proton exchange membrane fuel cell: A theoretical development, J. Comput. Multiph. Flows 9 (1) (2017) 3–25, http://dx.doi.org/10.1177/1757482X17692341.

[18] A.R. Sangtabi, A. Kianifar, E. Alizadeh, Effect of water vapor condensation on the flow distribution in a pem fuel cell stack, Int. J. Heat Mass Transfer 151 (2020) 119471, http://dx.doi.org/10.1016/j.ijheatmasstransfer.2020.119471, URL: https://www.sciencedirect.com/science/article/pii/S0017931019360946.

[19] T.E. Springer, T.A. Zawodzinski, S. Gottesfeld, Polymer Electrolyte Fuel Cell Model, J. Electrochem. Soc. 138 (8) (1991) 2334–2342, http://dx.doi.org/10.1149/1.2085971.

[20] E. Carcadea, D. Ingham, I. Stefanescu, R. Ionete, H. Ene, The influence of permeability changes for a 7-serpentine channel pem fuel cell performance, Int. J. Hydrog. Energy 36 (16) (2011) 10376–10383, http://dx.doi.org/10.1016/j.ijhydene.2010.09.050.

[21] H. Edwards, M.P. Pereira, S. Gharaie, R. Omrani, B. Shabani, Computational fluid dynamics modelling of proton exchange membrane fuel cells: Accuracy and time efficiency, Int. J. Hydrog. Energy 50 (2024-01) 682–710, http://dx.doi.org/10.1016/j.ijhydene.2023.09.004, URL: https://linkinghub.elsevier.com/retrieve/pii/S0360319923045676.

[22] European Commission. Joint Research Centre, Development of Reference Hardware for a Harmonised Testing of PEM Single Cell Fuel Cells, Publications Office, LU, 2021.

[23] A. d'Adamo, L. Martoccia, F. Berni, S. Breda, An analytical methodology to maximize the fuel cells system efficiency using optimal cathodic pressure and flow rate, Int. J. Hydrog. Energy 87 (2024) 159–170, http://dx.doi.org/10.1016/J.IJHYDENE.2024.09.018, Publisher: Pergamon.

[24] M.B. Satterfield, J.B. Benziger, Non-fickian water vapor sorption dynamics by nafion membranes, J. Phys. Chem. B 112 (12) (2008-03-01) 3693–3704, http://dx.doi.org/10.1021/jp7103243, URL: https://pubs.acs.org/doi/10.1021/jp7103243.

[25] J.T. Gostick, M.W. Fowler, M.D. Pritzker, M.A. Ioannidis, L.M. Behra, In-plane and through-plane gas permeability of carbon fiber electrode backing layers, J. Power Sources 162 (1) (2006-11) 228–238, http://dx.doi.org/10.1016/j.jpowsour.2006.06.096, URL: https://linkinghub.elsevier.com/retrieve/pii/S0378775306012596.